Combined Modelling and Experimental Studies of Failure in Thick Laminates under Out-of-Plane

Shear

L. Jia[1, 2], L. Yu[1], K. Zhang[1], M. Li [1, 2], Y. Jia[2], B.R.K. Blackman[1], J. P. Dear[1, *]

(1. Department of Mechanical Engineering, Imperial College London, South Kensington Campus, London SW7 2AZ, UK)

(2. First Aircraft Institute of AVIC, No. 1 Renmindong Road, Yanliang District, Xi'an, Shanxi 710089, P.R. China)

Abstract: A multi-scale model validated with out-of-plane shear testing is presented to analyse thick composite structural failure. Key features of this multi-scale analysis approach are inclusion of shear non linearity and modelling the response at a sub-laminate level whilst the structural failure is predicted at a ply level. Based on this multi-scale approach, a user-defined FORTRAN subroutine (VUMAT) has been written for ABAQUS/EXPLICIT solver and is used to model the shear nonlinearity and intra-laminar failure. In addition, a cohesive zone model is used to predict the inter-laminar delamination. The modelling has been employed to predict the failure processes for Iosipescu shear test specimens with different fibre orientations. The results show that both the failure mode and the load-displacement trace for finite element simulations agree closely with the experimental findings. This demonstrates the validity of this multi-scale, nonlinear, three-dimensional model for thick laminates. In particular, for the Iosepescu shear test, the effect of the fibres being aligned along the length of the specimen or out-of-plane is investigated as well as different dimensions of the specimen. These simulations are validated by experiments using Digital Image Correlation (DIC).

---

* Corresponding author. Tel.: t44-20-7594-7086; fax: t44-20-7823-8845.

E-mail address: j.dear@imperial.ac.uk (J.P. Dear), j.dear@ic.ac.uk (J.P. Dear).

1 Introduction

For thick-sectioned composite laminates, the ratio of span over thickness is relatively small and out-of-plane effects cannot be ignored. As a result, classical sheet or shell theory is inapplicable. Therefore, three-dimensional modelling and three-dimensional failure criteria should be employed. Although most commercial finite element software has already integrated analysis modules for composite structures, many of these are based on the classical two-dimensional laminate theory or three-dimensional ply-by-ply modelling [1,2,3]. For composite laminates with hundreds of layers, a three-dimensional ply-by-ply FEA model would be too time-consuming for both pre-processing and calculation.

For three-dimensional failure criterion, several solutions based on meso-mechanics [4, 5, 6] and macro-mechanics [7, 8, 9, 10] were proposed in The Second World-Wide Failure Exercise (WWFE-II). In these analyses, most employ a ply-by-ply approach except for Bogetti's multi-scale theory [10]. Bogetti's multi-scale theory is based on sub-laminate homogenization and decomposition of sub-laminate stress and strain [11]. With this method, the number of elements in the thickness direction of a laminate could be greatly reduced, and it is quite suitable for modelling thick composite laminates. Based on this multi-scale approach, several kinds of user subroutines were developed to solve thick laminate problems [12]. In these subroutines, the tangent stiffness is used to calculate the nonlinear shear stresses. In this approach, a very small load increment is required to calculate the stresses but the tangent stiffness method is not self-correcting and numerical errors can be accumulated. Also, when using the above subroutines, a database file which contains material and layup information will repeatedly be read from the local hard disk of a computer or server [13,14]. Reading data in this way is inefficient and would cause reading errors when multiple processors are used for parallel computing.

This paper presents an improvement to the above multi-scale approach. Chou's equivalent theory [15] is employed to calculate the equivalent elastic constants of the sub-laminates and the self-correcting secant

stiffness is used to describe the shear non-linearity. A user-defined material subroutine VUMAT is written for the ABAQUS/EXPLICIT solver. To integrate efficiently with the VUMAT subroutine and to improve the efficiency of reading the material and layup information, both were saved in individual FORTRAN parameter code files instead of being saved in a local text file. The parameter code is called with the "include" function not with the "read" function. In this way, the material and layup information can be obtained directly from computer memory, which is much more efficient than reading data from the hard disk. Moreover, this method could be used in parallel computing without introducing any error. With these improvements to the multi-scale approach, problems associated with large-scale complex thick-sectioned laminated structures can be solved efficiently as described in this paper.

2 Multi-scale modelling of stress-strain behaviour

2.1 The multi-scale approach

The multi-scale approach combines the macroscopic ply and the sub-laminate level (see Figure 1). In this case, an entire thick laminate is divided into several sub-laminates in the thickness direction. In each sub-laminate, there are a number of plies. For each sub-laminate, the equivalent stiffness must be firstly calculated with material mechanical properties and the layup information. After this calculation, the equivalent stiffness is used to calculate the general response of the entire structure, e.g. the global sub-laminate level displacements, stresses and strains. Then, the local ply level stresses and strains in the material coordinate system are obtained through coordinate transformation and decomposition of sub-laminate level stresses and strains. Finally, the ply level stresses and strains are used to predict the damage status and the corresponding stiffness reduction after damage occurs. This procedure is shown in Figure 1(a). In order to compare the difference between the current multi-scale modelling and the traditional ply-by-ply modelling, the procedure of ply-by-ply analysis is also supplied (see Figure 1(b)).

2.2 3D equivalent stiffness

According to Chou's 3D equivalent theory [15], a sub-laminate comprised of a number of plies with different ply angle or different materials is equivalent to a monolithic material with an equivalent stiffness matrix as follows:

$$
\left[\bar{C}_{ij}^* \right] =
\begin{bmatrix}
\bar{C}_{11}^* & \bar{C}_{12}^* & \bar{C}_{13}^* & 0 & 0 & \bar{C}_{16}^* \\
 & \bar{C}_{22}^* & \bar{C}_{23}^* & 0 & 0 & \bar{C}_{26}^* \\
 & & \bar{C}_{33}^* & 0 & 0 & \bar{C}_{36}^* \\
 & & & \bar{C}_{44}^* & \bar{C}_{45}^* & 0 \\
 & sym & & & \bar{C}_{55}^* & 0 \\
 & & & & & \bar{C}_{66}^*
\end{bmatrix}
\tag{1}
$$

where the barred notation "‾" is used to indicate that the stiffness coefficient is in the global coordinate system of the laminate and the star "*" signifies that it is an equivalent value. The stress-strain constitutive relationship for the sub-laminate is described as:

$$
[\bar{\sigma}^*] = [\bar{C}_{ij}^*][\bar{\varepsilon}^*]
\tag{2}
$$

where $\left[\bar{\sigma}^* \right]$ and $\left[\bar{\varepsilon}^* \right]$ are the global equivalent stresses and strains.

The coefficients of the sub-laminate stiffness matrix, $\bar{C}_{ij}^*$, are defined in Equations 3 to 6:

$$
\bar{C}_{ij}^* = \sum_{k=1}^{n} V^k \left[\bar{C}_{ij}^k - \frac{\bar{C}_{i3}^k \bar{C}_{3j}^k}{\bar{C}_{33}^k} + \frac{\bar{C}_{i3}^k \sum_{l=1}^{n} \dfrac{V^l \bar{C}_{3j}^k}{\bar{C}_{33}^k}}{\bar{C}_{33}^k \sum_{l=1}^{n} \dfrac{V^l}{\bar{C}_{33}^k}} \right] \quad (i,j=1,2,3,6)
\tag{3}
$$

$$
\bar{C}_{ij}^* = \bar{C}_{ji}^* = 0 \quad (i=1,2,3,6;\ j=4,5)
\tag{4}
$$

$$
\bar{C}_{ij}^* = \frac{\displaystyle\sum_{k=1}^{n} \frac{V^k}{\Delta_k} \bar{C}_{ij}^k}{\displaystyle\sum_{k=1}^{n}\sum_{l}^{n} \frac{V^k V^l}{\Delta_k \Delta_l} \left(\bar{C}_{44}^k \bar{C}_{55}^l - \bar{C}_{45}^k \bar{C}_{54}^l \right)} \quad (i,j=4,5)
\tag{5}
$$

$$
\Delta_k = \bar{C}_{44}^k \bar{C}_{55}^k - \bar{C}_{45}^k \bar{C}_{54}^k
\tag{6}
$$

where k refers to the kth ply of the sub-laminate, n refers to the number of plies in the sub-laminate, V^k is the ratio of the original thickness of the kth ply to the original total thickness of the entire sub-laminate

5

and $\overline{C}_{ij}^k$ represents the stiffness coefficient of the kth ply in a sub-laminate in the global coordinate system. This is obtained from the coordinate transformation of the stiffness matrix in the local material coordinate system [16].

2.3 Stress and strain decomposition

With the global equivalent stiffness, the general response of the entire structure, e.g. global stresses $\left[\overline{\sigma}^*\right]$ and strains $\left[\overline{\varepsilon}^*\right]$ can be easily obtained. However, all these values are in the sub-laminate level. In order to decompose the ply level stresses and strains, the following assumptions are introduced [10]:

$$\overline{\varepsilon}_i^k = \overline{\varepsilon}_i^* \quad (i=1,2,6; k=1,2,\cdots,n) \tag{7}$$

$$\overline{\sigma}_i^k = \overline{\sigma}_i^* \quad (i=3,4,5; k=1,2,\cdots,n) \tag{8}$$

where $\overline{\sigma}_i^k$ and $\overline{\varepsilon}_i^k$ are the stress and strain components for the kth ply in the global coordinate system, and $\overline{\sigma}_i^*, \overline{\varepsilon}_i^*$ refer to the stress and strain components for the sub-laminate in the global coordinate system. With the above assumptions, all the remaining ply level stress and strain components can be obtained from Equations 9 and 10:

$$\begin{bmatrix} \overline{\varepsilon}_3^k \\ \overline{\varepsilon}_4^k \\ \overline{\varepsilon}_5^k \end{bmatrix} = \begin{bmatrix} \overline{C}_{33}^k & \overline{C}_{34}^k & \overline{C}_{35}^k \\ \overline{C}_{43}^k & \overline{C}_{44}^k & \overline{C}_{45}^k \\ \overline{C}_{53}^k & \overline{C}_{54}^k & \overline{C}_{55}^k \end{bmatrix}^{-1} \begin{bmatrix} \overline{\sigma}_3^k \\ \overline{\sigma}_4^k \\ \overline{\sigma}_5^k \end{bmatrix} - \begin{bmatrix} \overline{C}_{31}^k & \overline{C}_{32}^k & \overline{C}_{36}^k \\ \overline{C}_{41}^k & \overline{C}_{42}^k & \overline{C}_{46}^k \\ \overline{C}_{51}^k & \overline{C}_{52}^k & \overline{C}_{56}^k \end{bmatrix} \begin{bmatrix} \overline{\varepsilon}_1^k \\ \overline{\varepsilon}_2^k \\ \overline{\varepsilon}_6^k \end{bmatrix} \quad (k=1,2,\cdots,n) \tag{9}$$

$$\begin{bmatrix} \overline{\sigma}_1^k \\ \overline{\sigma}_2^k \\ \overline{\sigma}_6^k \end{bmatrix} = \begin{bmatrix} \overline{C}_{11}^k & \overline{C}_{12}^k & \overline{C}_{13}^k & \overline{C}_{14}^k & \overline{C}_{15}^k & \overline{C}_{16}^k \\ \overline{C}_{21}^k & \overline{C}_{22}^k & \overline{C}_{23}^k & \overline{C}_{24}^k & \overline{C}_{25}^k & \overline{C}_{26}^k \\ \overline{C}_{61}^k & \overline{C}_{62}^k & \overline{C}_{63}^k & \overline{C}_{64}^k & \overline{C}_{65}^k & \overline{C}_{66}^k \end{bmatrix} \begin{bmatrix} \overline{\varepsilon}_1^k \\ \overline{\varepsilon}_2^k \\ \overline{\varepsilon}_3^k \\ \overline{\varepsilon}_4^k \\ \overline{\varepsilon}_5^k \\ \overline{\varepsilon}_6^k \end{bmatrix} \quad (k=1,2,\cdots,n) \tag{10}$$

As this stage, all the ply level stresses and strains in the global coordinate system have been obtained. However, before using them to predict the failure status of each ply, they have to be transformed from the global coordinate system to the local material coordinate system.

2.4 Non-linear shear constitutive response

For in-plane or out-of-plane shear in a laminate, the non-linear response can be determined in a number of ways [8]. In the present research, the shear nonlinearity in each ply is represented by using the Ramberg-Osgood constitutive equation [17]. Taking the non-linear stress-strain relationship between τ_{13} and γ_{13} as an example, it is defined as:

$$\tau_{13} = \frac{G^0_{13}\gamma_{13}}{\left(1+\left(\frac{G^0_{13}\gamma_{13}}{S_{13}}\right)^n\right)^{\frac{1}{n}}} \tag{11}$$

and the secant modulus G^s_{13} is obtained by the following equation [17]:

$$G^s_{13} = \frac{\tau_{13}}{\gamma_{13}} = \frac{G^0_{13}}{\left(1+\left(\frac{G^0_{13}\gamma_{13}}{S_{13}}\right)^n\right)^{\frac{1}{n}}} \tag{12}$$

where G^0_{13} refers to the initial undamaged shear modulus, S_{13} is the shear strength and *n* is the shape factor of the nonlinear stress-strain curve. The parameter *n* is determined by fitting to the experimental data to a power-law as shown in Figure 2.

3. Progressive failure modelling

3.1 Failure criterion

For in-plane fibre tensile and compressive failure, the simple maximum-stress criterion has been used [8,18,19, 20]:

$$f_{ft} = \frac{\sigma_{11}}{X_T} \qquad (\sigma_{11} \geq 0) \tag{13}$$

$$f_{fc} = -\frac{\sigma_{11}}{X_C} \qquad (\sigma_{11} < 0) \tag{14}$$

where X_T and X_C are the axial tensile and compressive strength.

For matrix failure, the following equations have been used to calculate the normal traction σ_n and the shear tractions τ_L and τ_T in the potential fracture plane [21]:

$$\sigma_n = \frac{\sigma_{22} + \sigma_{33}}{2} + \frac{\sigma_{22} - \sigma_{33}}{2}\cos(2\varphi) + \tau_{23}\sin(2\varphi) \tag{15}$$

$$\tau_T = -\frac{\sigma_{22} - \sigma_{33}}{2}\sin(2\varphi) + \tau_{23}\cos(2\varphi) \tag{16}$$

$$\tau_L = \tau_{12}\cos(\varphi) + \tau_{13}\sin(\varphi) \tag{17}$$

where ϕ is the fracture angle as shown in Figure 3.

For matrix compressive failure ($\sigma_n < 0$), the following criterion has been used [21]:

$$f_{mc} = \left(\frac{\tau_T}{S_T - \mu_T\sigma_n}\right)^2 + \left(\frac{\tau_L}{S_L - \mu_L\sigma_n}\right)^2 \qquad (\sigma_n < 0) \tag{18}$$

where S_L and S_T are the longitudinal and transverse (to the fibres) shear strengths, μ_L and μ_T are longitudinal and transverse friction coefficients which have been obtained from the following equations:

$$\mu_T = -\frac{1}{\tan(\phi_0)} \tag{19}$$

$$\mu_L = S_L\frac{\mu_T}{S_T} \tag{20}$$

The longitudinal shear strength, S_L, is obtained from a shear test, whilst the transverse shear strength, S_T, is calculated from the compressive strength in the matrix direction, Y_C and the fracture angle for pure matrix compression, ϕ_0 (typically, $\phi_0 \approx 53°$) [21]:

$$S_T = Y_C\cos(\phi_0)\left(\sin(\phi_0) + \frac{\cos(\phi_0)}{\tan(2\phi_0)}\right) \tag{21}$$

For matrix tensile failure ($\sigma_n \geq 0$), the quadratic stress criterion has been employed [21]:

$$f_{mt} = \left(\frac{\sigma_n}{Y_t}\right)^2 + \left(\frac{\tau_T}{S_T}\right)^2 + \left(\frac{\tau_L}{S_L}\right)^2 \qquad (\sigma_n \geq 0) \tag{22}$$

3.2 Damage evolution

For fibre failure, the damage variable d_f is given by:

$$d_f = 1 - (1 - d_{ft})(1 - d_{fc}) \tag{23}$$

where

$$d_{ft}(\varepsilon_{11}) = \frac{\varepsilon_{f,1}^t}{\varepsilon_{f,1}^t - \varepsilon_{0,1}^t}(1 - \frac{\varepsilon_{0,1}^t}{\varepsilon_{11}}) \qquad (24)$$

$$d_{fc}(\varepsilon_{11}) = \frac{\varepsilon_{f,1}^c}{\varepsilon_{f,1}^c - \varepsilon_{0,1}^c}(1 - \frac{\varepsilon_{0,1}^c}{\varepsilon_{11}}) \qquad (25)$$

The superscripts t and c refer to tension and compression, respectively, $\varepsilon_{0,1}^t$ and $\varepsilon_{0,1}^c$ correspond to the

strain in tension and compression when the failure initiation appears, $\varepsilon_{f,1}^t$ and $\varepsilon_{f,1}^c$ correspond to the

maximum strain in tension and compression at final failure, i.e. when the damage variables are equal to

one. The maximum failure strain $\varepsilon_{f,1}^t$ and $\varepsilon_{f,1}^c$ are then obtained by:

$$\varepsilon_{f,1}^t = \frac{2G_{IC}^t}{X_T L} \qquad (26)$$

$$\varepsilon_{f,1}^c = \frac{2G_{IC}^c}{X_C L} \qquad (27)$$

where X_T and X_C are the tensile and compressive strengths in fibre direction, G_{IC}^t and G_{IC}^c are the

intra-laminar fracture toughness in fibre tension and compression and L is the characteristic length of

an element. In the present research, all the hexahedral elements (see Figure 4) used in the potential

failure area are with equal in-plane length, so the characteristic length, L, has been obtained by:

$$L = \sqrt{\frac{V}{T}} \qquad (28)$$

where V is the volume of an element and T is the dimension in the thickness direction of an element as

shown in Figure 4(a). The stress–strain behaviour in fibre tension and compression before and after

damage are depicted in Figure 4(b).

When the energy-based damage evolution criterion is used, there is a lower limit to the permissible

element size that can be used, otherwise, for very coarse meshes ($L \rightarrow \infty$) and ε_f tends to zero [21].

For matrix failure, the critical strain energy release rate for matrix fracture is much smaller than that of

fibre fracture, so the element size has to be limited to be very small. For thick-sectioned laminates, and

FEA model with too many small elements is unacceptable due to its low efficiency. Therefore, in

matrix failure analysis, a parametric damage evolution method is typically used to replace the

energy-based damage evolution. When $f_{mt} \geq 1$, the damage variable for matrix tensile failure d_{mt} is set

to zero, or when $f_{mc} \geq 1$, the damage variable for matrix compressive failure d_{mc} is set to 0.6, as was

shown to be suitable in [22,23], the damage variable d_m is given by:

$$d_m = 1\text{-}(1\text{-}d_{mt})(1\text{-}d_{mc}) \tag{29}$$

When damage occurs in the kth ply and the fracture angle ϕ for matrix failure equals to zero, the stiffness

matrix for this damage ply is updated by

$$\mathbf{C}_d^k = \begin{bmatrix} (1-d_f)C_{11}^0 & (1-d_f)(1-d_m)C_{12}^0 & (1-d_f)C_{13}^0 & 0 & 0 & 0 \\ (1-d_f)(1-d_m)C_{12}^0 & (1-d_m)C_{22}^0 & (1-d_m)C_{23}^0 & 0 & 0 & 0 \\ (1-d_f)C_{13}^0 & (1-d_m)C_{23}^0 & C_{33}^0 & 0 & 0 & 0 \\ 0 & 0 & 0 & (1-d_m)C_{44}^0 & 0 & 0 \\ 0 & 0 & 0 & 0 & (1-d_f)C_{55}^0 & 0 \\ 0 & 0 & 0 & 0 & 0 & (1-d_f)(1-d_m)C_{66}^0 \end{bmatrix}$$

$$\tag{30}$$

where C_{ij}^0 is the undamaged stiffness coefficient in the local material coordinate system.

When damage occurs in a ply and the fracture angle ϕ for matrix failure does not equal to zero, the

stiffness matrix is firstly transformed from the local material coordinate system to the fracture coordinate

system, and then the stiffness coefficients in the fracture coordinate system are all discounted. Then, the

damaged stiffness matrix is transformed back from the fracture coordinate system to the local material

coordinate system. In this paper, this transformation of the stiffness matrix is used for both matrix tensile

and compressive failure, for which the fracture angle is usually not equal to zero.

After the damaged stiffness matrix for the kth ply in local material coordinate system C_d^k is obtained,

then it is then transformed from the local material coordinate system to the global coordinate system in

order to get the globally damaged stiffness matrix, $\bar{C}_d^k$, after that, Equations 5 to 8 are employed to calculate the global damaged equivalent stiffness matrix for one sub-laminate, $\bar{C}_d^*$.

For thick laminated structures, it is not efficient to monitor and save the damage variables for each ply, as this would consume a large amount of computation time and storage space. A much better approach has been followed in this work using the concept of the stiffness ratio for the sub-laminate, as discussed in [10-12]. It then follows that:

$$R_{ij} = \frac{\bar{C}_{ij}^{c,*}}{\bar{C}_{ij}^{0,*}} \quad (i, j = 1, 6) \tag{31}$$

where R_{ij} is the stiffness ratio, $\bar{C}_{ij}^{0,*}$ refers to the equivalent undamaged stiffness coefficient in the global coordinate system at the beginning of loading, and $\bar{C}_{ij}^{c,*}$ is the current equivalent damaged or discounted stiffness coefficient in global coordinate system. The initial valve of each stiffness ratio is one. At the beginning of each load increment, all the stiffness ratios are used to update the current stiffness coefficients, whilst, at the end of each load increment, the up-to-date stiffness radios are calculated and saved according to the current damage status. In this way, a major saving in computational time and storage space is achieved.

4 Comparison of simulation with experimental results

4.1 Validation of multi-scale approach

Two virtual composite laminates ([0$_4$] and [0/90]$_s$) measuring 20×10×0.5 mm^3 were used to evaluate the performance of the multi-scale model. The laminates were continuously loaded in the fibre direction under displacement control (see Figure 5). The material properties for the composite (CCF300/5228A) were selected as shown in Table 1, and the thickness of a single ply was taken as 0.125mm [24, 25].

For comparison purposes, the load-displacement responses for the composite panel obtained using

multi-scale modelling and traditional ply-by-ply modelling are represented on a single graph in Figure 5. All the computation has been implemented by using the same number of CPUs and under the same hardware conditions. The loading velocity in each FEA model is also the same. Figure 5(a) compares the structural response obtained by using the two different modelling approaches for laminate with stacking sequence $[0_4]$. Correspondingly, Figure 5(b) compares the structural response for laminate with stacking sequence $[0/90]_s$. Table 1 gives the mechanical properties of the composite laminates evaluated in this paper as quoted by the prepreg manufacturer and Table 2 compares the accuracy and computing efficiency for the two different modelling methods for the $[0_4]$ and $[0/90]_s$ stacks sequences.

From Figure 5, the load versus displacement trace for the current multi-scale modelling and traditional ply-by-ply modelling are similar. Table 2 also gives the first peak load and the maximum load obtained from the two methods which are also similar. This demonstrates that the accuracy of multi-scale modelling is acceptable. Moreover, the stable time increment for the multi-scale modelling is much larger than that for ply-by-ply modelling. With such a larger stable time increment and relatively fewer finite elements, the current multi-scale modelling is much more efficient in calculation than that of the traditional ply-by-ply modelling.

4.2 Out-of-plane shear test and simulation for thick laminates

Six variants of Iosipescu shear specimens (see Figure 6) with different fibre orientation (G13 shear test and G23 shear test) and different out of plane thickness or specimen height, h, were designed according to the ASTM D5379 standard [26]. These experiments are presented in more detail in the PhD dissertation of Long Yu [27]. The cutting directions for the G13 and G23 shear test specimen are shown in Figure 6(a) and the Iosipescu test fixture is shown in Figure 6(b). For the G13 shear test specimen (see Figure 6 (c)), the fibres are along the longitudinal direction of the specimen, while for the G23 shear test, the fibres are

along the transverse direction of the specimen (see Figure 6 (d)).

For each specimen, (with 160 plies), the dimension, d_1, is 20 mm and the entire laminate is divided into 20 sub-laminates through this direction, each sub-laminate is modelled with C3D8R elements. For the G13 shear test, 5 layers of cohesive elements (COH3D8) were used to model the delamination [28]. The dimensions of the specimens are given in Figures 6(c) and 6(d).

Material properties were taken from Table 1 and Table 3 gives the inter-laminar stiffness, strength and fracture toughness for the cohesive zone model as used in the modelling. The G13 shear test results are shown in Figure 7 for when the fibres are in the longitudinal direction. The shear test specimens were continuously loaded under displacement control and the full field strain fields were measured using 3D Digital Image Correlation (DIC). The G13 & G23 shear tests are firstly presented for specimens with out-of-plane thickness or specimen height, h=5 mm and they are then compared with specimens of height, h=8 mm and h=3 mm.

For the G13 shear test (h=5 mm), Figure 7 shows the experimental load-displacement curve for Experiment 1 (Figure 7(a)), load-displacement traces for Experiments1, 2, 3 and 4 (Figure 7(b)), a comparison with FEA (Figure 7(c)) and strain fields from DIC (Figure 7 (d)) and FEA (Figure 7(e)).

In Figure 7 (a), position Ⓐ refers to the beginning of loading, where both the load and displacement are near zero. The position Ⓑ is approximately at the middle of the linear portion, the strain concentration on the specimen appears in two areas, one is at the bottom of the V-notch and another is at the contact area near the edge of the loading fixture. At the position Ⓒ, the first two cracks caused by delamination appear at the bottom of the two V-notches, accompanied with the first load drop on the load-displacement curve. With an increase in the displacement, the cracks continue to propagate, then, at the position Ⓓ, the second two cracks appear, which are nearly parallel to the initial cracks, correspondingly, accompanied with the second load drop on the load-displacement curve. The loading curve between

13

position Ⓒ and position Ⓓ is slightly non-linear. As the displacement continues to increase, the reaction load gradually reaches its peak point, and then a number of cracks begin to appear in the middle of the two notches, at the same time, the third load drop on the load-displacement curve appears, shown as position Ⓔ. After this point, with a further increase in displacement, the reaction load increases slightly and then gradually decreases. Due to the constraint of the fixture, a maximum of 2 mm displacement was set to protect the fixture.

Three further specimens (Experiment 2, Experiment 3, and Experiment 4) were evaluated to confirm the reproducibly of the experiments and the results are shown in Figure 7(b). Figure 7(c) compares the simulated load-displacement curves with the experimental data for Experiment 2. Both the linear multi-scale model and the non-linear multi-scale model have been used to predict the structural response of the specimen.

It can be seen that the load-displacement curve obtained from the non-linear multi-scale model is a closer fit to the experiments than the linear model. For the first peak load, the error between non-linear multi-scale model and the average experimental results is less than 1%, whilst the error in the linear multi-scale model is less than 5%. For the maximum load, the error in the non-linear multi-scale model is less than 5%, whilst the error for the linear multi-scale model is larger than 10 %. It is clear that, for the G13 shear test, the non-linear effect of the material on the structural response is significant and cannot be ignored.

Figures 7 (d) and 7 (e) show the comparison of failure mode and maximum principal strain from DIC and non-linear FEA at the five positions (Ⓐ to Ⓔ) for the G13 shear test (h=5mm). It can be seen that the predicted onset of failure and the position of strain concentration are in good agreement with the experimental results from DIC. However, there is the notable difference for the position and value of the maximum principal strain in the strain plots. The reason for this difference is that, when damage is

14

initiated in the FEA model, the corresponding elements will be deleted in the FEA model so as to form the cracks, so the maximum principal strain becomes zero (this is the area shown as the white region in Figure 9(e) – see enlarged image). However, for the DIC strain plots, when a crack appears and the size of the crack is small, the strain value around the tip of the crack is very large (this is the area shown as red region in Figure 9(d)).

For the G23 shear test (h=5mm), Figure 8 shows the failure process in a similar way as in Figure 7. The load-displacement curve for Experiment 1 (see Figure 8(a)) is almost linear through the entire loading history. With the increase of the displacement, the load gradually reaches its peak value, and then two cracks appear and propagate very rapidly, accompanied with the load dropping dramatically (Position Ⓔ shown in Figure 8(a)).

Two further specimens (Experiment 2 and Experiment 3) were evaluated to confirm the experimental load-displacement traces. The results are shown in Figure 8(b). The average experimental load capacity for the G23 shear test is 2.55 kN and the maximum experimental load capacity is 2.8 kN whilst the predicted load capacity is 2.8 kN. The G23 shear test is quite sensitive to the manufacturing quality and the mating position of the specimen, which is the reason why the experimental results differ slightly.

Figure 8(c) shows the comparison of experimental load-displacement curve (Experiment 1) with predicted results from the non-linear multi-scale model. Since the rigs are modelled with rigid elements, the slope of the simulated load-displacement curve is higher than for the experimental result.

Figures 8(d) and 8(e) compare the failure mode and shear strain γ_{23} from DIC and non-linear FEA at five positions for the G23 shear test (h=5mm). The strain plot from FEA compares well with the experimental strain plots from DIC. Features such as the stress concentration position and the crack propagation path are numerically captured by the FEA model.

To demonstrate the versatility of the three-dimensional multi-scale modelling, experiments and FEA

analysis for G13 and G23 shear test were performed with two out of plane thicknesses or specimen heights (h=8 and 3 mm). Figure 9 (a) shows the load-displacement trace and failure mode for the G13 shear test (h=8 mm). The characteristic load-displacement trace and failure mode for the shear test with a height of 8 mm are similar with the results of the shear test with a height of 5 mm. Three specimens (Experiment 1, Experiment 2, and Experiment 3) were tested to confirm the experimental reproducibility and the results are shown in Figure 9 (b). Both the linear multi-scale model and the non-linear multi-scale model are used to predict the structural response of the specimen. As shown in Figure 9 (c), the comparison between experimental and simulated load-displacement curves confirms that, for the G13 shear test, the non-linear multi-scale model has a much higher accuracy than the linear model.

Figures 9 (d) and 9 (e) show the similar comparison of failure mode and maximum principal strain from DIC and non-linear FEA at the specified positions for the G13 shear test (h=8 mm). The failure mode and the position of strain concentration from FEA agrees well with experimental results from DIC. Again, for FEA when damage is initiated the corresponding elements are deleted to give the white region between the crack surfaces (Figure 9(e)). However, for the DIC strain plots, when a crack appears and the size of the crack is small, the strain value around the tip of the crack is very large and gives a red region (Figure 9(d)).

For G23 shear test (h=8 mm), the failure procedure as shown in Figure 10 is quite similar to the experimental result of the G23 shear test with a height of 5 mm. Three specimens (Experiment 1, Experiment 2 and Experiment 3) were evaluated and the load-displacements curves are shown in Figure 10 (b). The average experimental load capacity for the G23 shear test (h=8mm) is 4.3 kN, and the maximum experimental load capacity is 4.7 kN, whilst the predicted load capacity is 4.6 kN. The load-displacement curve of Experiment 3 is selected to compare with FEA simulated results (as shown in Figure 10 (c)).

Figures 10 (d) and 10 (e) compare the failure mode and shear strain γ_{23} from DIC and non-linear FEA at the five positions ((A) to (E)) for the G23 shear test (h=8 mm). The failure mode, the crack propagation path and the strain from FEA all agree well with experimental results from DIC.

Figures 11 and 12 shows the load-displacement trace and failure mode for G13 and G23 shear tests (h=3 mm). For G13, there were two specimens (Experiment 1 and Experiment 2) and for G23, there were three specimens (Experiment 1, Experiment 2 and Experiment 3). The characteristic load-displacement trace and failure mode for the shear test with a h=3 mm are similar as for h=8mm.

For all three out of plane thicknesses, the numerical simulation of the G23 shear test indicated that matrix failure due to tensile and shear tractions in the potential fracture plane is the dominant failure mode in the specimen. By introducing the appropriate failure criterion when predicting the potential fracture plane in the multi-scale analysis, the crack propagation path has been captured effectively.

5 Conclusions

Employing a progressive failure approach to thick-sectioned composite structures, a non-linear multi-scale methodology based on sub-laminate homogenization and decomposition of sub-laminate stresses and strains has been presented. The accuracy of this approach has been checked by comparing numerical predictions with experimental results for out-of-plane shear tests, and the efficiency of the multi-scale approach has been verified by comparing multi-scale modelling and traditional ply-by-ply modelling for a virtual composite specimen under uniaxial tensile loading. The model predicts the effects of fibre orientation for different out-of-plane dimensions (h = 3, 5 & 8 mm) with most of the failure features observed with good accuracy, e.g. failure mode, peak load and crack propagation path. The comparison between the linear model and the non-linear multi-scale models in predicting the structural

response of the G13 shear test shows that the non-linear material effect on the structural response is significant and the non-linear model is much more accurate than the traditional linear model.

The major findings of the present research can be summarised as follows:

- A user-defined material subroutine for a multi-scale composite material failure model has been developed and was employed in the simulation of the Iosipescu shear test.

- By comparing with ply-by-ply modelling, the efficiency and accuracy of the multi-scale modelling approach have been verified.

- The model was successfully employed to predict the effect of fibre orientation and the effect of varying the out-of-plane dimension in the Iosipescu shear test specimen.

- For the G13 specimens, the non-linear model accurately predicts the response of a structure subjected to shear load and the formation of delaminations at the notch root and through the specimen thickness.

- The G23 Iosipescu test is well represented by this multi-scale modelling approach with the position and onset of the shear crack accurately reproduced.

The non-linear multi-scale methodology based on sub-laminate homogenization developed in this paper is a useful design tool and has been employed by FAI and AVIC and will be helpful to other aircraft manufacturers of thick-sectioned composites subjected to shear load. The model developed can be effectively applied to realistic engineering applications e.g. pin-jointed and other metallic/composites jointed structures subjected to the shear and other mechanical loading.

References

[1] DS.SIMULIA.ABAQUS User Manual. Version 6.10, ABAQUS Inc., Providence, RI, USA, 2010.

[2] Hallquist J O. LS-DYNA theory manual. Livermore software Technology Corporation, 2006, 3.

[3] Dytran MSC. Theory manual. Wydawnictwo MSC, 2013.

[4] Zhou Y X, Huang Z M. A bridging model prediction of the ultimate strength of composite laminates subjected to triaxial loads. Journal of Composite Materials, 2012: 46: 2343–2378.

[5] Carrere N, Laurin F, Maire J F. Micromechanical-based hybrid mesoscopic 3D approach for non-linear progressive failure analysis of Failure models and criteria for frp under in-plane or three-dimensional stress states including shear non-linearity. Composite structure. Journal of Composite Materials, 2012, 46(19-20): 2389-2415.

[6] Nelson E E, Hansen A C, Mayes J S. Failure analysis of composite laminates subjected to hydrostatic stresses: A multicontinuum approach. Journal of Composite Materials, 2012, 46(19-20):

2461-2483.

[7] Hashin Z. Failure criteria for unidirectional fiber composites. Journal of applied mechanics, 1980, 47(2): 329-334.

[8] Pinho S T, Darvizeh R, Robinson P, Schuecker C, Camanho PP. Material and structural response of polymer-matrix   fibre-reinforced composites. Journal of Composite Materials, 2012, 46(19-20): 2313-2341.

[9] Deuschle H M, Puck A. Application of the Puck failure theory for fibre-reinforced composites under three-dimensional stress: Comparison with experimental results. Journal of Composite Materials, 2013, 47(6-7): 827-846.

[10] Bogetti T A, Staniszewski J, Burns B P, Hoppel C PR, Gillespie J W. Predicting the nonlinear response and progressive   failure of composite laminates under tri-axial loading. Journal of Composite Materials, 2012,46:   2443–2459.

[11] Bogetti, T A, Hoppel, C P R, Drysdale W H. Three-Dimensional Effective Property and Strength Prediction of Thick Laminated Composite Media. U.S. Army Research Laboratory: Aberdeen Proving Ground, MD, October 1995.

[12] Staniszewski J M, Bogetti T A, Keefe M. An Improved Design Methodology for Modeling Thick-Section Composite Structures Using a Multiscale Approach. U.S. Army Research Laboratory: Aberdeen Proving Ground, MD, 2012.

[13] Bogetti, T. A.; Hoppel, C.P.R.; Burns, B. P. LAMPAT: A Software Tool for Analyzing and Designing Thick Laminated Composite Structures; Technical Report 890; U.S. Army Research Laboratory: Aberdeen Proving Ground, MD, September 1995.

[14] Staniszewski J M, Bogetti T A. LAMPAT and LAMPATNL User's Manual. ARMY

RESEARCH LAB ABERDEEN PROVING GROUND MD WEAPONS AND MATERIALS

RESEARCH DIRECTORATE, 2012.

[15] Chou P C, Carleone J, Hsu C M. Elastic constants of layered media.Journal of Composite

Material,1972,6(1):80-93

[16] JIANG Yongqiu,LU Fengsheng,GU Zhijian. Composite Material Mechanics.Xi′an: Xi′an

Jiaotong University, October 1993

[17] Richard R M, Blacklock J R. Finite element analysis of inelastic structures. AIAA Journal,

1969,7:432-438

[18] Raimondo L, Iannucci L, Robinson P, Curtis P T. A progressive failure model for

mesh-size-independent FE analysis of composite laminates subject to low-velocity impact damage.

Composites Science and Technology, 2012, 72(5): 624-632.

[19] Donadon M V, Iannucci L, Falzon B G, Hodgkinson J M, Almeida S F M. A progressive failure

model for composite laminates subjected to low velocity impact damage. Computers & Structures,

2008, 86(11): 1232-1252.

[20] Faggiani A, Falzon B G. Predicting low-velocity impact damage on a stiffened composite panel.

Composites Part A: Applied Science and Manufacturing, 2010, 41(6): 737-749.

[21] Pinho S T, Iannucci L, Robinson P. Physically based failure models and criteria for laminated

fibre-reinforced composites with emphasis on fibre kinking. Part II: FE implementation. Composites

Part A: Applied Science and Manufacturing, 2006, 37(5): 766-777.

[22] Tserpes K I, Labeas G, Papanikos P, Kermanidis Th. Strength prediction of bolted joints in

graphite/epoxy composite laminates. Composites Part B: Engineering, 2002, 33(7): 521-529.

[23] Labeas G, Belesis S, Stamatelos D. Interaction of damage failure and post-buckling behaviour of

composite plates with cut-outs by progressive damage modelling. Composites Part B: Engineering, 2008, 39(2): 304-315.

[24] Han G, Guan Z, Ji Z, Du S. Initial damage induced by thermal residual stress and microscopic failure analysis of carbon-fiber reinforced composite under shear loading. Composite Interfaces, 2015 (ahead-of-print): 1-15.

[25] Private communication, AVIC Beijing Institute of Aeronautical Materials, December 2011.

[26] Standard, A. S. T. M. "Standard test methods for shear properties of composite materials by the V-notched beam method." West Conshohocken (PA): ASTM100 (1997).

[27] Yu Long, Mechanical properties for composite materials for aerospace applications, PhD Dissertation, Imperial College London, October 2016.

[28] Turon A, Davila C G, Camanho P P, Costa J. An engineering solution for mesh size effects in the simulation of delamination using cohesive zone models. Engineering fracture mechanics, 2007, 74(10): 1665-1682.
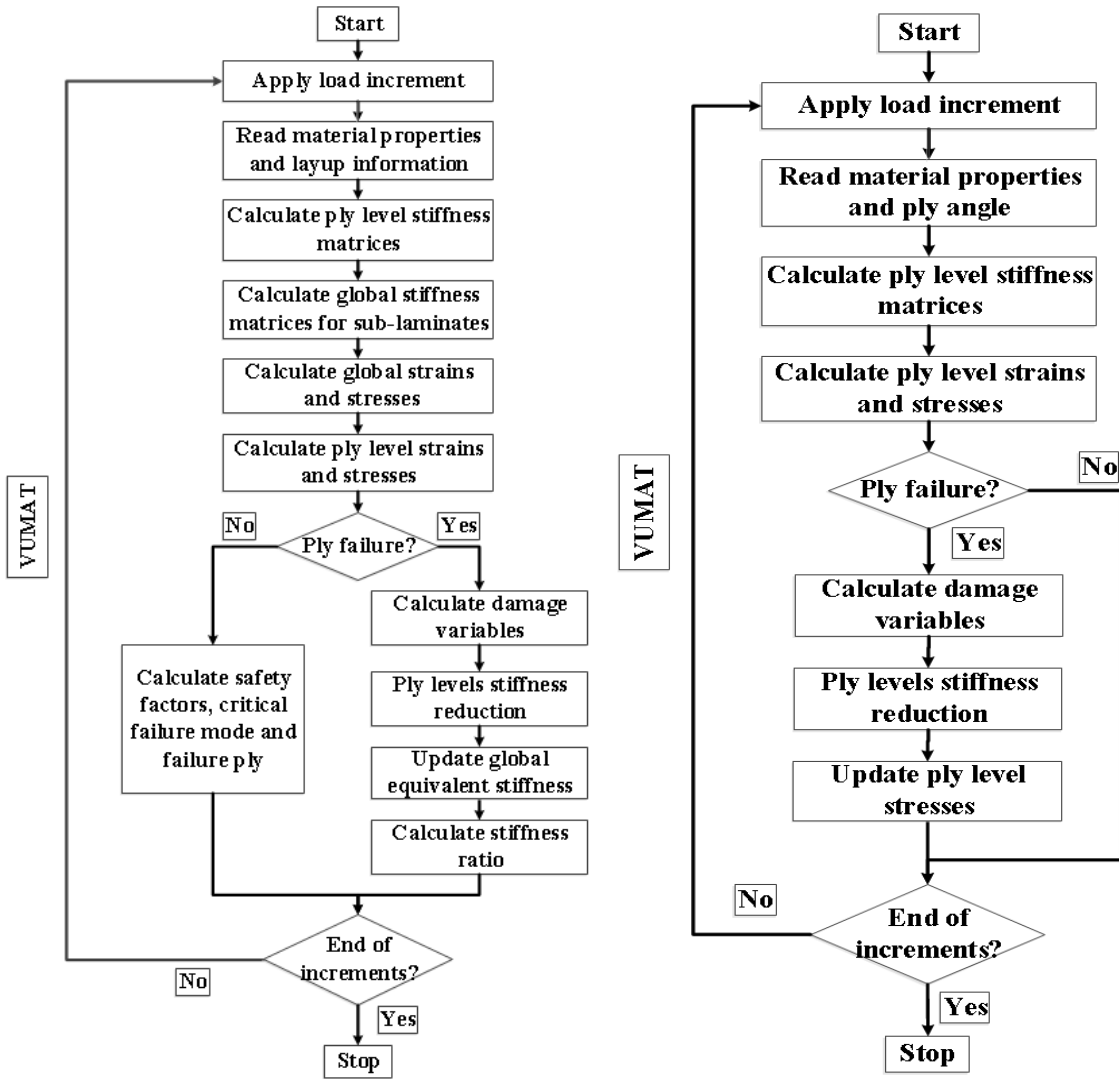
(a) Multi-scale modelling   (b) Ply-by-ply modelling

Figure 1. Procedure for multi-scale and ply-by-ply modelling.
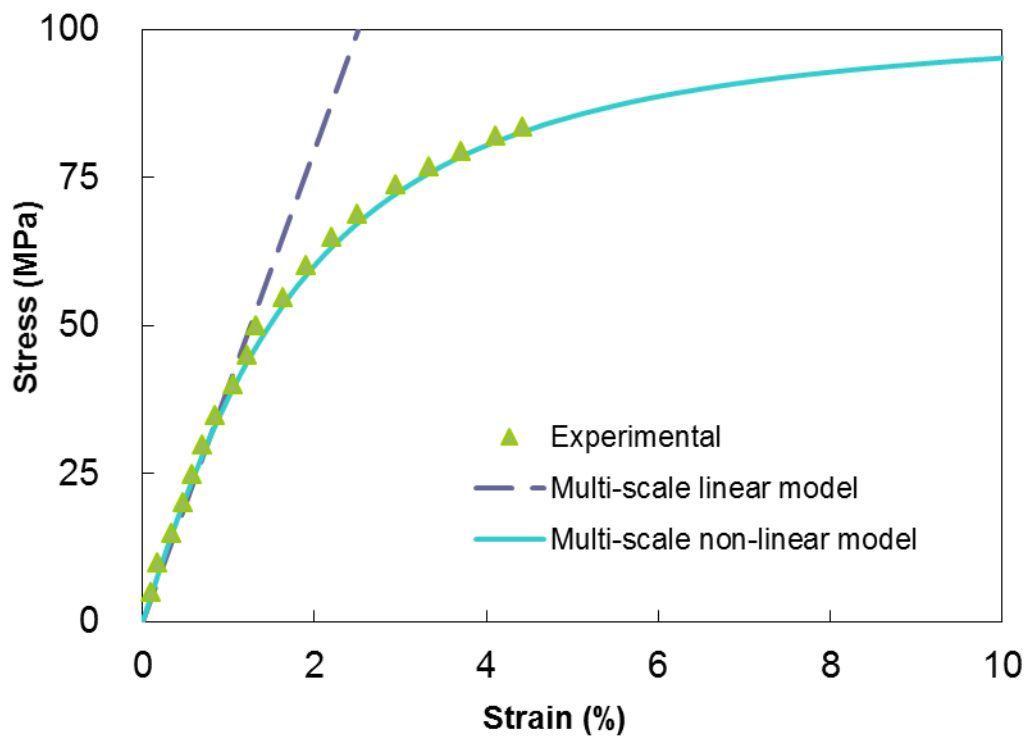
Figure 2. Non-linear stress-strain relationship and the effect of shape factor.
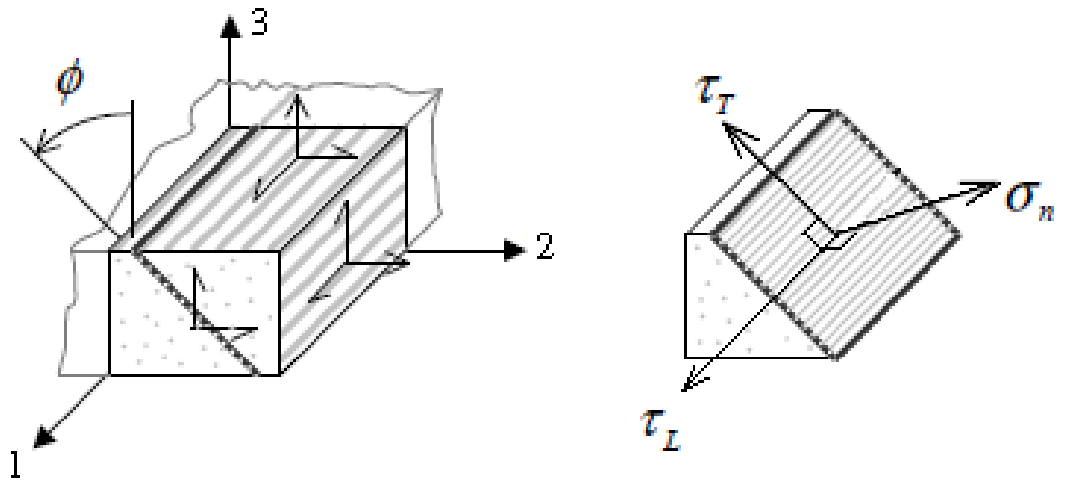
Figure 3. Fracture plane for a 3D stress state and the associated stresses.
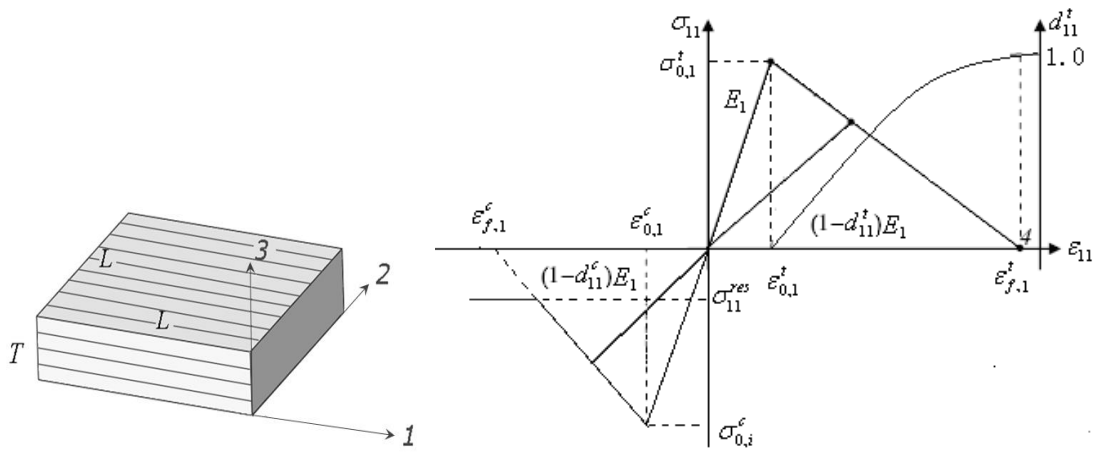
(a) Characteristic length of an element   (b) Material behaviour in the longitudinal direction.

Figure 4. Determination of the characteristic length and the longitudinal material behaviour.
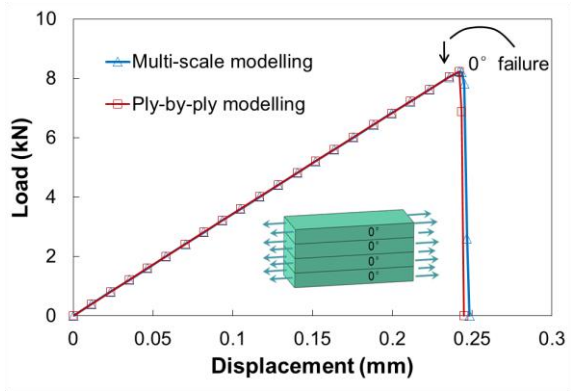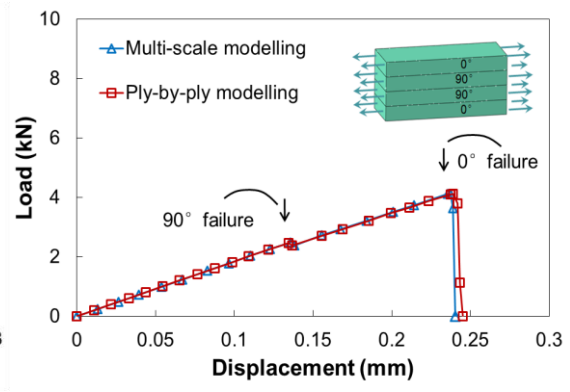
(a) [0₄]   (b) [0/90]ₛ

Figure 5. Validation of multi-scale modelling as compared with ply-by-ply modelling.
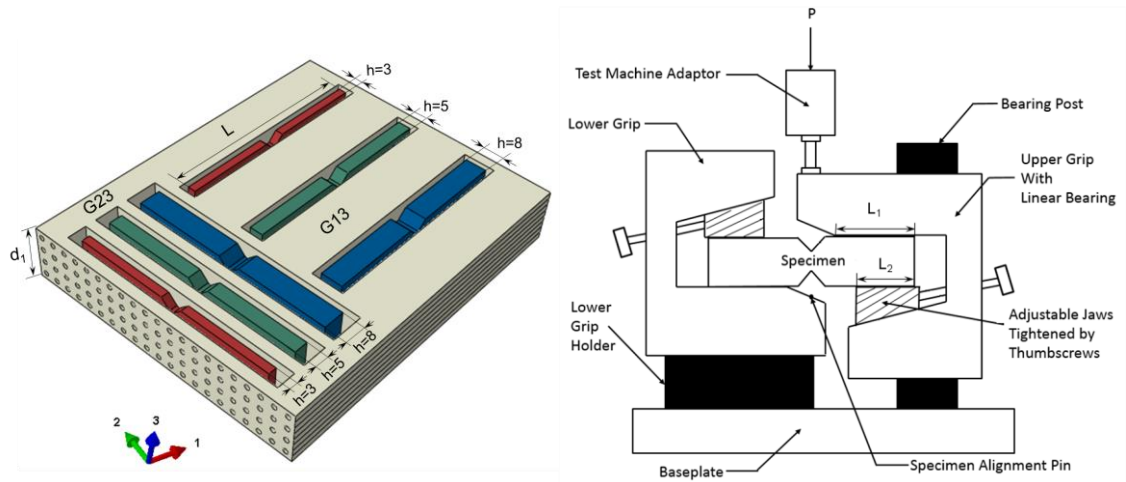
(a) Schematic diagram for specimen   (b) V-Notched beam test fixture schematic for Iosipescu shear test
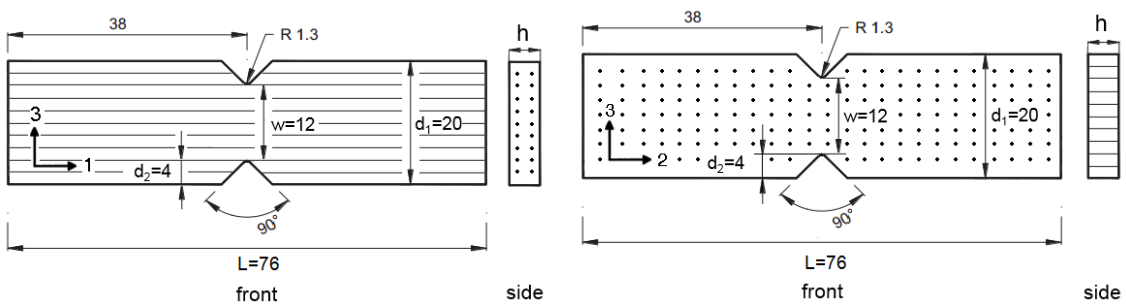
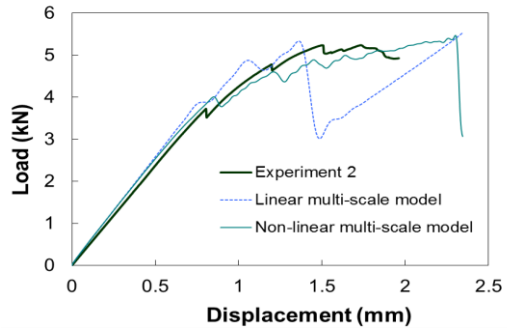(c) Dimensions for G13 shear test specimen   (d) Dimensions for G23 shear test specimen

Figure 6. Specimen dimensions and test fixture schematic for Iosipescu shear test (dimensions in mm).
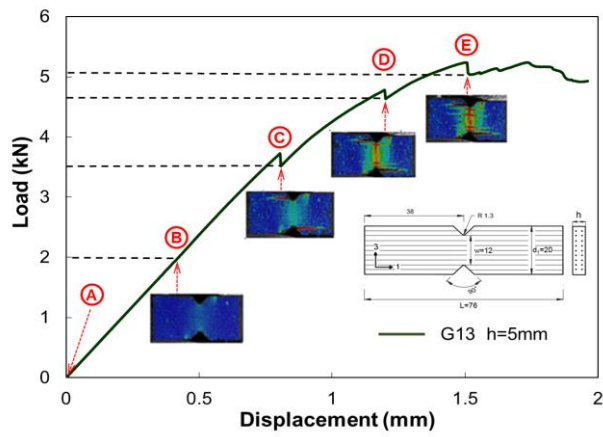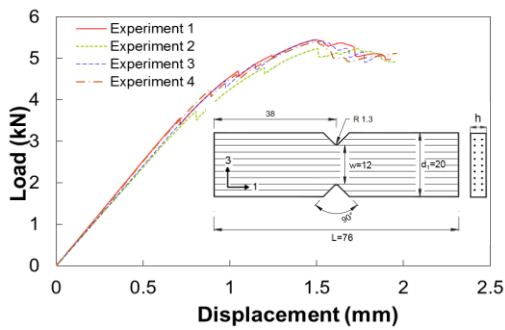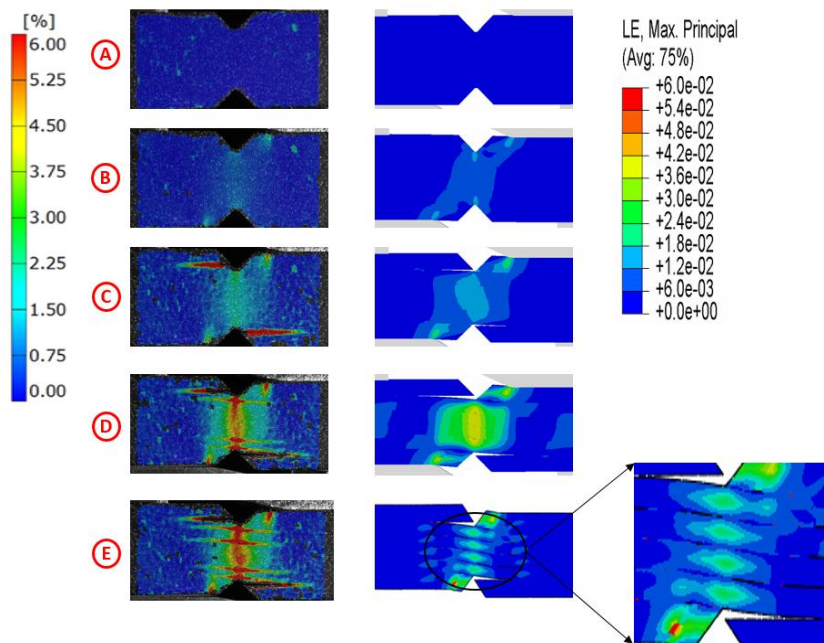
Figure 7. Comparison of experimental and simulated results for G13 shear test (h=5mm): (a) Load-displacement trace and failure mode; (b) Load versus displacement trace; (c) Comparison of experimental and simulated load-displacement traces; (d) Failure mode and maximum principal strain from DIC; (e) Failure mode and maximum principal strain from FEA.
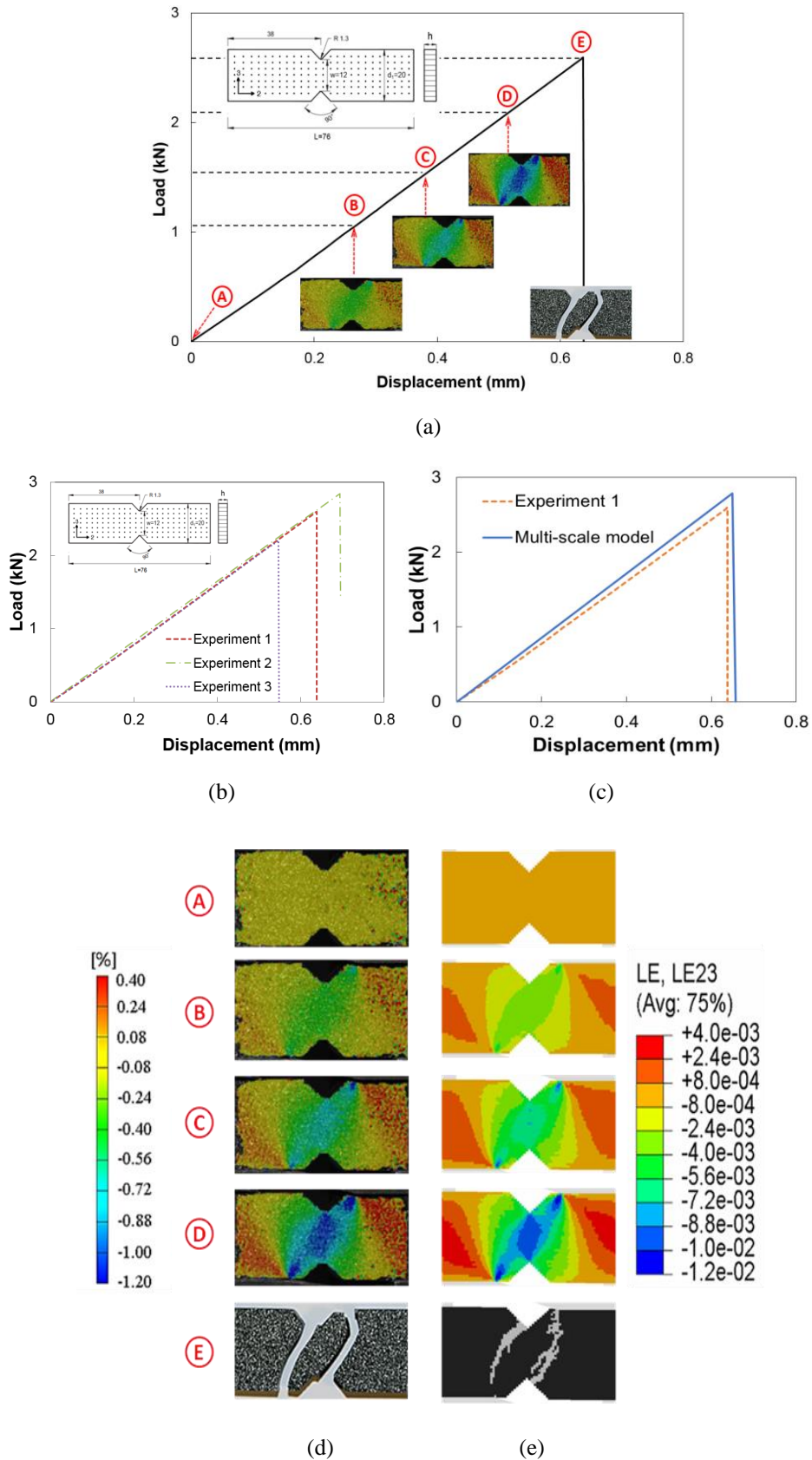
(a)

(b)

(c)

(d)

(e)

Figure 8. Comparison of experimental and simulated results for G23 shear test (h=5mm): (a) Load-displacement trace and failure mode; (b) Load versus displacement trace; (c) Comparison of experimental and simulated load-displacement traces; (d) Failure mode and γ_{23} from DIC; (e) Failure mode and γ_{23} from FEA.
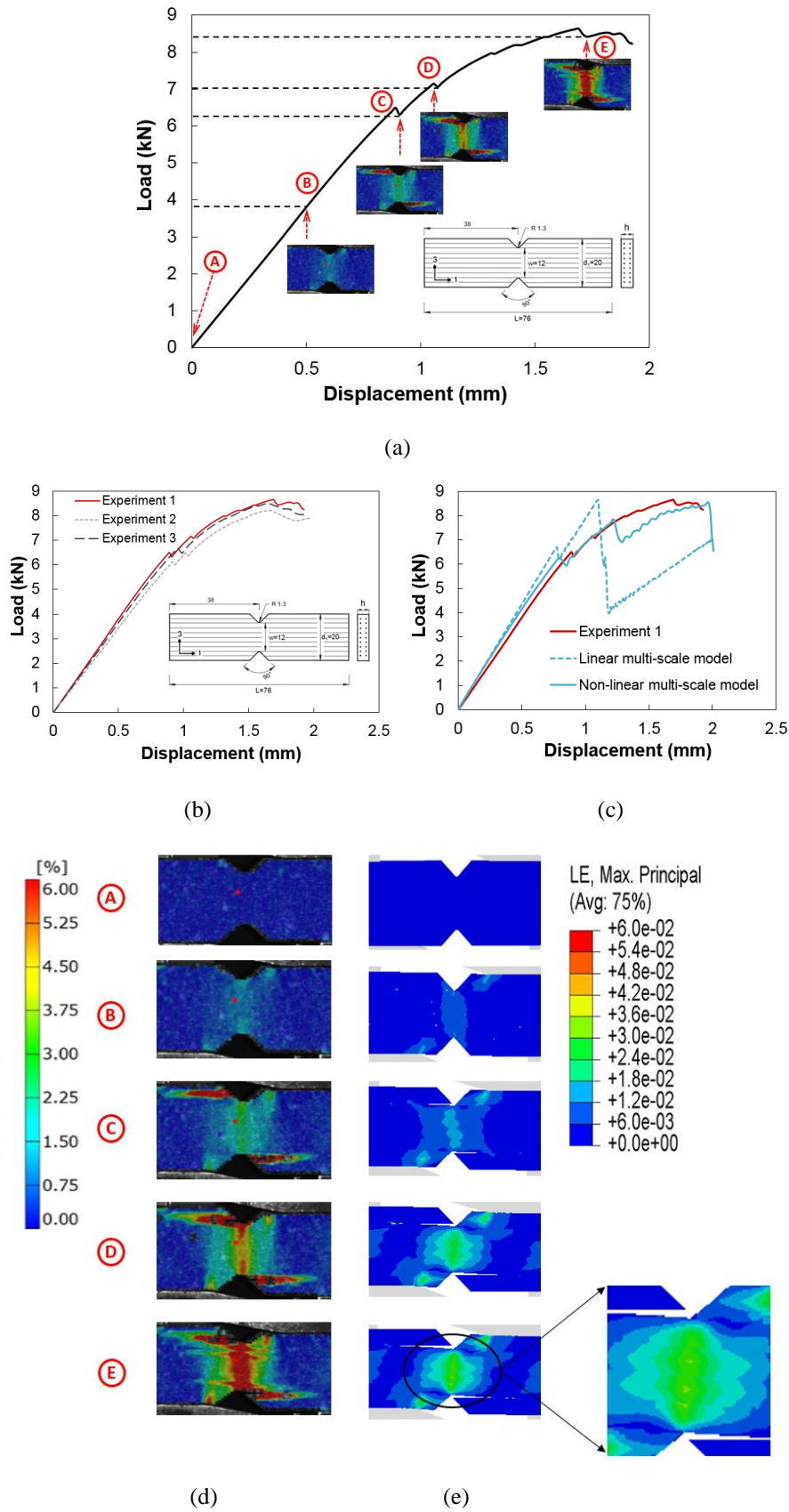
Figure 9. Comparison of experimental and simulated results for G13 shear test (h=8mm): (a) Load-displacement trace and failure mode; (b) Load versus displacement trace; (c) Comparison of experimental and simulated load-displacement traces; (d) Failure mode and maximum principal strain from DIC; (e) Failure mode and maximum principal strain from FEA.
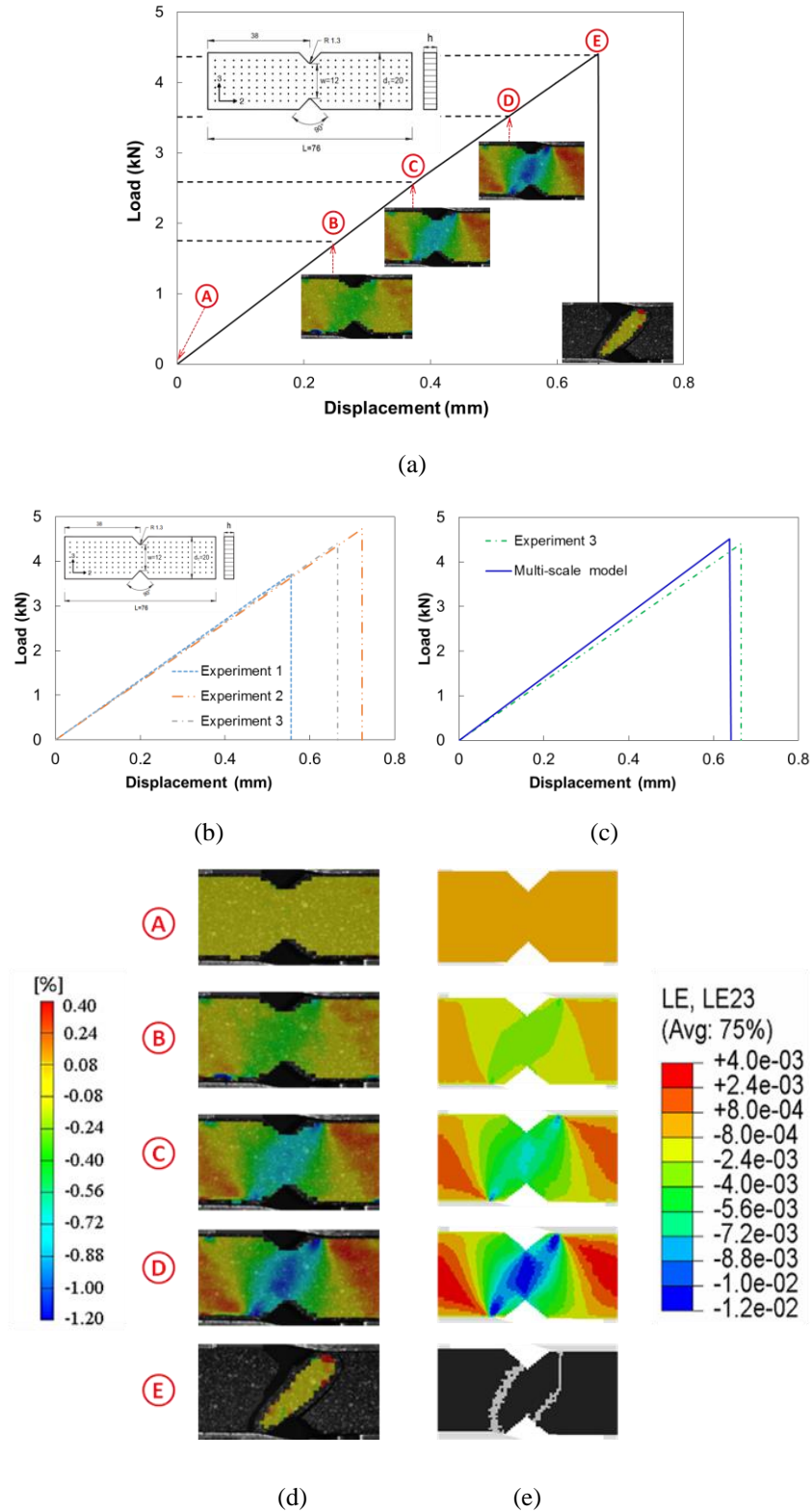
(a)

(b)   (c)

(d)   (e)

Figure 10. Comparison of experimental and simulated results for G23 shear test (h=8mm): (a) Load-displacement trace and failure mode; (b) Load versus displacement trace; (c) Comparison of experimental and simulated load-displacement traces; (d) Failure mode and γ_{23} from DIC; (e) Failure mode and γ_{23} from FEA.
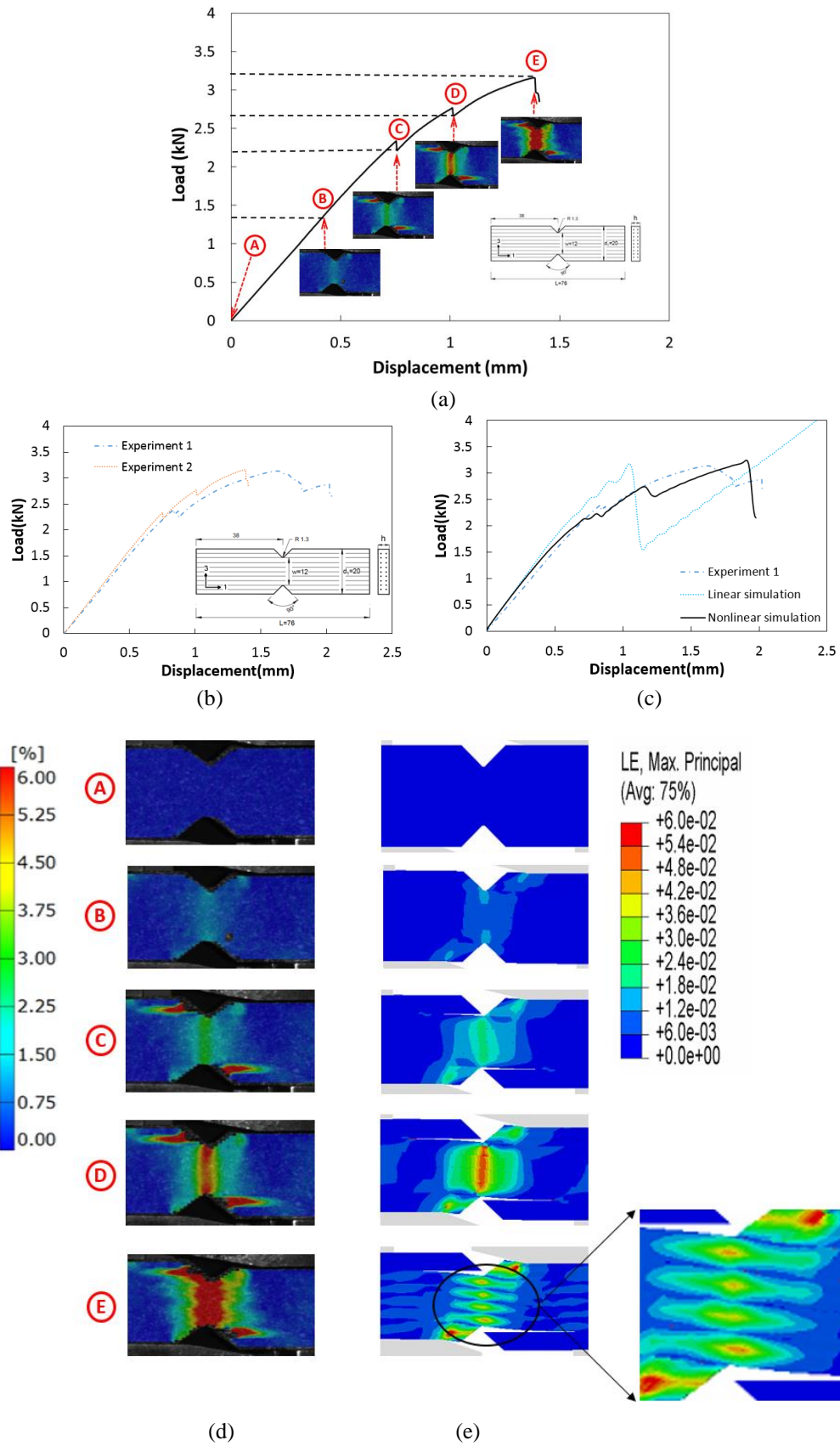
Figure 11. Comparison of experimental and simulated results for G13 shear test (h=3mm): (a) Load-displacement trace and failure mode; (b) Load versus displacement trace; (c) Comparison of experimental and simulated load-displacement traces; (d) Failure mode and maximum principal strain from DIC; (e) Failure mode and maximum principal strain from FEA.
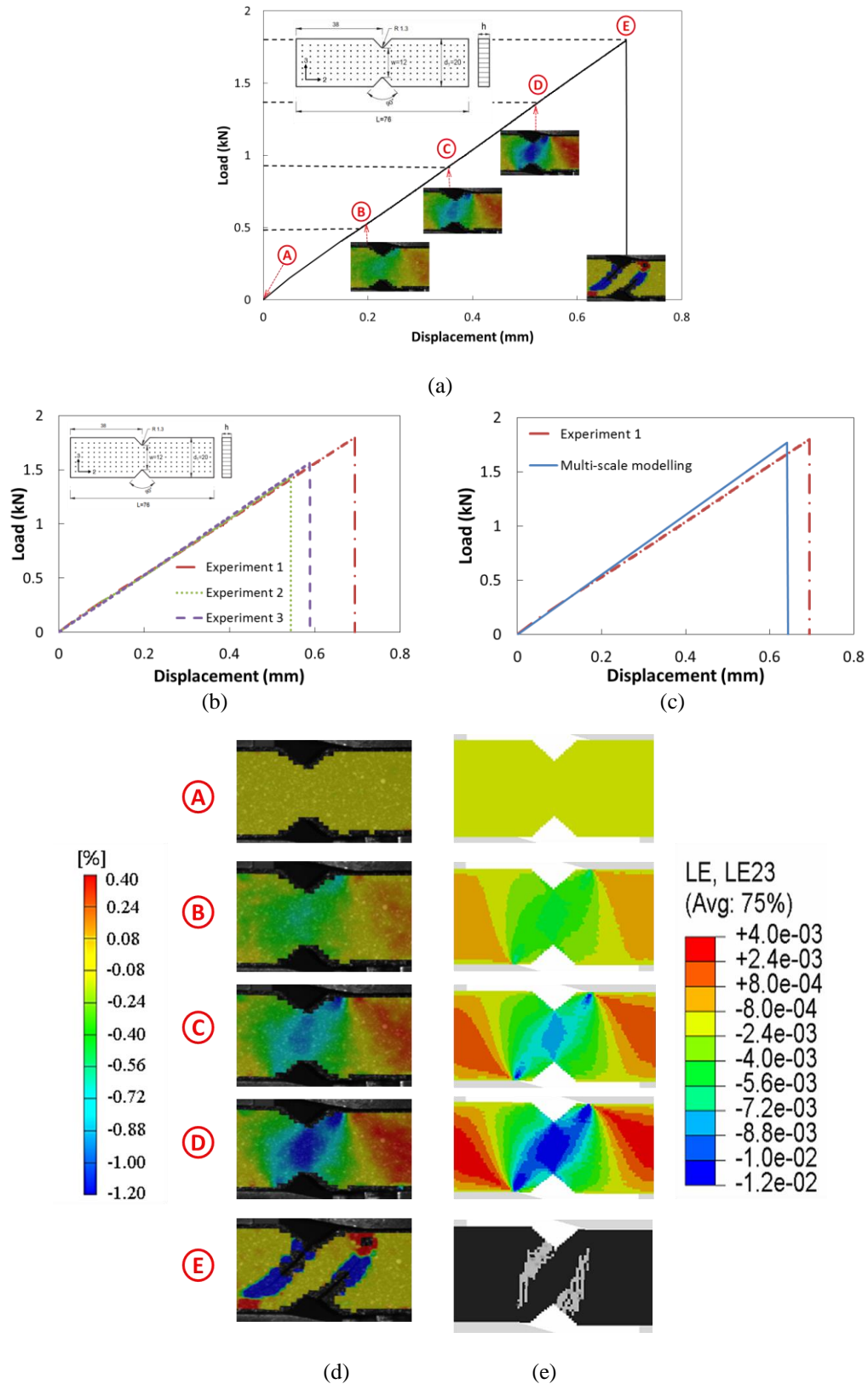
Figure 12. Comparison of experimental and simulated results for G23 shear test (h=3mm): (a) Load-displacement trace and failure mode; (b) Load versus displacement trace; (c) Comparison of experimental and simulated load-displacement traces; (d) Failure mode and γ_{23} from DIC; (e) Failure mode and γ_{23} from FEA.

Table 1. Mechanical property of uni-axial laminates.

E_1 (MPa)	E_2 (MPa)	E_3 (MPa)	υ_{12}	υ_{13}	υ_{23}	G_{12} (MPa)	G_{13} (MPa)	G_{23} (MPa)
138000	9040	9040	0.307	0.307	0.35	4500	4500	3476
X_T (MPa)	X_C (MPa)	Y_T (MPa)	Y_C (MPa)	S_L (MPa)	S_T (MPa)	n	G_{12}^0 (MPa)	G_{13}^0 (MPa)
1696	1188	71.4	202	102	90	1.3	4500	4500

Table 2. Comparison of accuracy and computing efficiency for different analysis methods.

Stacking sequence	Modelling Type	First peak load(N)	Maximum Load(N)	Stable Time Increment
[0$_4$]	Multi-scale		8221.00	1.87299e-07
	Ply-by-ply		8238.46	4.83202e-08
[0/90]$_s$	Multi-scale	2489.91	4108.59	1.87299e-07
	Ply-by-ply	2490.92	4144.41	4.83202e-08

Table 3. Inter-laminar stiffness, strength and fracture toughness of composite laminate for Iosipescu shear tests.

E (MPa)	G (MPa)	N_0 (MPa)	S_0 (MPa)	T_0 (MPa)	G_{IC} （N/mm）	G_{IIC} （N/mm）	G_{IIIC} （N/mm）
9000	4500	71.4	102	102	0.75	1.5	1.5